JACS Au
AN OPEN ACCESS JOURNAL OF THE AMERICAN CHEMICAL SOCIETY

pubs.acs.org/jacsau
Article

Reactive Capture and Conversion of CO_2 into Hydrogen over Bifunctional Structured $Ce_{1-x}Co_xNiO_3$/Ca Perovskite-Type Oxide Monoliths

Khaled Baamran, Shane Lawson, Ali A. Rownaghi,* and Fateme Rezaei*

Cite This: *JACS Au* 2024, 4, 101−115
Read Online

ACCESS | Metrics & More | Article Recommendations | Supporting Information

ABSTRACT: Carbon capture, utilization, and storage (CCUS) technologies are pivotal for transitioning to a net-zero economy by 2050. In particular, conversion of captured CO_2 to marketable chemicals and fuels appears to be a sustainable approach to not only curb greenhouse emissions but also transform wastes like CO_2 into useful products through storage of renewable energy in chemical bonds. Bifunctional materials (BFMs) composed of adsorbents and catalysts have shown promise in reactive capture and conversion of CO_2 at high temperatures. In this study, we extend the application of 3D printing technology to formulate a novel set of BFMs composed of CaO and $Ce_{1-x}Co_xNiO_3$ perovskite-type oxide catalysts for the dual-purpose use of capturing CO_2 and reforming CH_4 for H_2 production. Three honeycomb monoliths composed of equal amounts of adsorbent and catalyst constituents with varied $Ce_{1-x}Co_x$ ratios were 3D printed to assess the role of cobalt on catalytic properties and overall performance. The samples were vigorously characterized using X-ray diffraction (XRD), energy-dispersive spectroscopy (EDS), N_2 physisorption, X-ray photoelectron spectroscopy (XPS), H_2-TPR, *in situ* CO_2 adsorption/desorption XRD, and NH_3-TPD. Results showed that the $Ce_{1-x}Co_x$ ratios—x = 0.25, 0.50, and 0.75—did not affect crystallinity, texture, or metal dispersion. However, a higher cobalt content reduced reducibility, CO_2 adsorption/desorption reversibility, and oxygen species availability. Assessing the structured BFM monoliths via combined CO_2 capture and CH_4 reforming in the temperature range 500−700 °C revealed that such differences in physiochemical properties lowered H_2 and CO yields at higher cobalt loading, leading to best catalytic performance in $Ce_{0.75}Co_{0.25}NiO_3$/Ca sample that achieved 77% CO_2 conversion, 94% CH_4 conversion, 61% H_2 yield, and 2.30 H_2/CO ratio at 700 °C. The stability of this BFM was assessed across five adsorption/reaction cycles, showing only marginal losses in the H_2/CO yield. Thus, these findings successfully expand the use of 3D printing to unexplored perovskite-based BFMs and demonstrate an important proof-of-concept for their use in combined CO_2 capture and utilization in H_2 production processes.

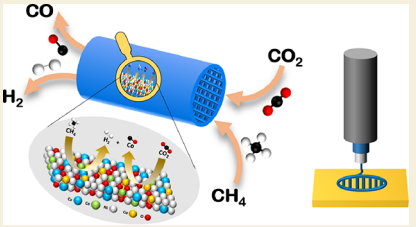

KEYWORDS: *reactive capture of CO_2, bifunctional materials, structured monolith, methane dry reforming, hydrogen production*

1. INTRODUCTION

It is well-recognized that anthropogenic CO_2 emissions are contributing greatly to climate change, and significant efforts are underway to curtail such emissions and to limit the global temperature rise to 1.5 °C by 2050.[1−3] Unfortunately, capturing and storing CO_2 is still unattractive from an industrial point-of-view, as this greenhouse contaminant is usually mitigated by amine scrubbing or by reaction with CaO at high temperatures to form $CaCO_3$.[4,5] Both of these processes have drawn substantial criticisms as they constantly consume chemical resources without any true revenue stream, since the market price of CO_2 is only $20/t, which is lower than the energy costs associated with either of these mitigation strategies.[6] Hence, more energy-efficient and affordable methods of handling CO_2 emissions are required for long-term economic sustainability.

In recent years, a shift in perspective on CO_2 has started to occur, as the greenhouse gas is being viewed less as a harmful contaminant and more as a potential feedstock for catalytic processes.[7,8] For example, we have previously demonstrated CO_2 as an oxidizing agent in processes such as oxidative dehydrogenation of propane (ODHP)[9,10] or ethane (ODHE).[11] Similarly, Sutthiumporn et al.[12] demonstrated CO_2 as a potential feedstock to generate H_2 over perovskite catalysts by way of dry methane reforming (DMR). The use of CO_2 in H_2 production is a particularly interesting route, since this process generates both H_2 and CO, otherwise known as syngas.[13,14] Syngas synthesis is particularly noteworthy since its constituents can act as building blocks for other processes in Fischer−Tropsch syntheses, which include potential liquid fuel sources such as methanol, thereby allowing the greenhouse gas to be used cyclically in a marketable manner, while addressing

Received: September 18, 2023
Revised: November 19, 2023
Accepted: November 22, 2023
Published: December 13, 2023

its poor economic value and providing a pathway toward mitigation.[15,16] Nevertheless, the thermodynamic stability of CO_2 is quite high, implying that development of efficient catalytic materials for its transformation into syngas is paramount.[17,18]

Generally speaking, the thermodynamic stability of CO_2 forces its conversion into syngas to be performed at high temperatures. For instance, Mette et al.[19] demonstrated dry reforming of methane at high temperatures (800−900 °C) for efficient conversion of CO_2 into syngas. Accordingly, these extreme reaction conditions incur high energy costs—which ultimately incur a CO_2 penalty unless the system is powered by renewables—leading to the benefits of CO_2 repurposing being offset by these intrinsic disadvantages. Recently, a subclass of catalytic materials, consisting of mixed metal oxide phases and capable of acting as both acidic and basic catalysts, has gained significant attention for its potential in CO_2 conversion via DMR reaction.[20−22] This is mainly because they enable conversion into syngas at considerably lower temperatures. The key advantage of these materials lies in their mixed active sites, which facilitate multiple reaction pathways to occur at the same time. This approach is more entropically favorable compared to single-path conversion, particularly in terms of producing thermodynamically stable species.[23] For example, Sastre at al.[24] demonstrated $La_{1-x}Sr_xFeO_3$ perovskite-type catalysts for methane reforming with CO_2-splitting reactions through varying the ratio of Sr/La (A-site), and reported that the Sr phase leads to promoting the surface oxygen species whereas the La phase concurrently leads to leveling off this property when the Sr/La ratio is sufficiently low. As another benefit, such synergism allows both the oxidation and reduction reactions to progress in a manner that avoid carbon deposition (coking), thus providing exceptional on-stream stability.[25−28] In another example,[12] the effectiveness of $La_{0.8}Sr_{0.2}Ni_{0.8}M_{0.2}O_3$ catalysts (M = Bi, Co, Cr, Cu, Fe) for CO_2-DMR was demonstrated and it was shown that substituting Fe for Ni (B-site) enhances catalytic stability by (i) strengthening metal−support interactions to hinder Ni agglomeration and (ii) increasing the lattice oxygen availability in the $La_2O_2CO_3$ intermediate phase to block coke formation pathways.[12] Of course, these are just a handful of examples—with many more being present in the literature—[18,29,30]so the benefit of combining active sites in catalysts is quite clear for CO_2-utilizing applications.

This being stated, CO_2 capture and its subsequent utilization are often relegated to being performed in multiple beds, as the former step generally occurs at far lower temperatures than the later step.[5] As a byproduct of this thermal gradient, whose energy input incurs CO_2 penalties unless powered by a renewable or nuclear source, CO_2 conversion rates tend to be undesirably low. Indeed, such penalties are exacerbated when considering factors of steam heating, column cooling, and overall process control.[31−33] Because of such issues, there have been significant efforts put forth to allow CO_2 capture and subsequent utilization to occur in a singular bed since this would eliminate (or minimize) the thermal swing, thus lowering total energy consumption and enhancing overall process throughput. The culmination of such efforts has led to the development of so-called "bifunctional materials" (BFMs), which are composed of (i) a catalyst phase and (ii) a high-temperature adsorbent phase (CaO). Such BFMs have been employed in a myriad of lab-scale proof-of-concept demonstrations with highly promising results, including dry methane reforming,[34] ODHE,[35,36] ODHP,[9,10] and more.[37−41]

Even in such instances, an underlying deficit remains, which should be considered for scaling these materials. Namely, the current focus on BFM materials has focused solely on synthesizing powdered catalysts, with no significant effort being allocated toward structuring the composite. Granted, the latter aspect cannot be implemented without the former, but such BFMs must be structured to prevent powder attrition and to reduce column restrictions. We have recently shown that BFMs—heterogeneous catalysts—can be easily processed into honeycomb contactors via binding with a ceramic binder (i.e., bentonite clay), followed by 3D printing and calcination.[42−46] In such processes, the premade catalyst is combined with $CaCO_3$, which is phase transitioned into CaO by calcination to generate the adsorbent phase. A successful proof-of-concept—which could reasonably be transitioned to scalable production via conventional ram- or screw-extrusion techniques—3D printing BFMs by this manner has been shown to generate favorable reaction kinetics due to the open honeycomb design, as well as high cyclic stability and good retention of catalyst physiochemical properties (surface area, redox properties, crystallinity, etc.).[47] However, the application of this technology has been limited solely to that in our earlier works, which were focused entirely on alkane dehydrogenation. It can be reasonably expected that implementing CO_2 capture and conversion at an industrial scale will require diversification across various reactions, considering the broad scope of commodity chemical refining. Therefore, it is important to extend this technique to previously unexplored areas to further cement the promise of structured BFM honeycomb monoliths.

Motivated by this need, we embarked on a study of 3D-printed BFMs composed of CaO adsorbent and $Ce_{1-x}Co_xNiO_3$ perovskite-type oxide catalysts for the process of capturing CO_2 and utilizing in H_2 production via DMR process. The $Ce_{1-x}Co_xNiO_3$ catalysts were first synthesized using a previously reported method in the literature,[12] which used citric acid as a complexing agent and involved substituting the A-site (Ce) with B-site (Co) in the perovskite structure $CeNiO_3$. This method resulted in the growth of different phases such as $NiCo_2O_4$, NiO, and CeO_2 metal oxides, alongside the $CeNiO_3$ perovskite. The $CeNiO_3/NiCo_2O_4/NiO/CeO_2$ catalysts were synthesized through a one-step procedure and then combined with CaO adsorbent during the process of 3D printing for fabrication of BFM monoliths. For this purpose, the $Ce_{1-x}Co_x$ ratio was systematically varied to assess its impact on the performance of BFMs in CO_2 capture and utilization during DMR reaction, across a range of adsorption-reaction temperatures. *In situ* X-ray diffraction experiments were conducted to examine the reversibility of CO_2 adsorption−desorption runs at high temperatures. The materials in this study—which to our knowledge were the first structured $CeNiO_3/NiCo_2O_4/NiO/CeO_2/CaO$ BFMs—demonstrated promising performance in the DMR reaction as well as exceptional on-stream stability. Such efforts enable new and exciting pathways through which to utilize CO_2, thus bringing capture/conversion technology one step closer to utilization at-scale.

https://doi.org/10.1021/jacsau.3c00553
JACS Au 2024, 4, 101−115

Table 1. Masses of Metal Precursors (g) Used for Catalyst Synthesis

catalyst	x (g)	$Ce(NO_3)_3{\cdot}6H_2O$ (g)	$(CH_3COO)_2Co{\cdot}4H_2O$ (g)	$Ni(NO_3)_2{\cdot}6H_2O$ (g)	citric acid (g)
CCN-1	0.25	0.75	0.25	1.75	2.75
CCN-2	0.50	0.50	0.50	1.75	2.75
CCN-3	0.75	0.25	0.75	1.75	2.75

2. EXPERIMENTAL SECTION

2.1. Materials

The following chemicals were used for BFMs synthesis without further purification: nickel(II) nitrate hexahydrate ($Ni(NO_3)_2{\cdot}6H_2O$) (99%), cerium(III) nitrate hexahydrate ($Ce(NO_3)_3{\cdot}6H_2O$) (99%), cobalt(II) acetate tetrahydrate ($(CH_3COO)_2Co{\cdot}4H_2O$) (99%), citric acid (ACS reagent, >99.5%), calcium carbonate ($CaCO_3$) (99%), bentonite clay (99%), and methylcellulose (99%). All these materials were purchased from Sigma-Aldrich. The ultrahigh purity (UHP) gases used in this study were obtained from Airgas.

2.2. Synthesis of Catalysts

$Ce_{1-x}Co_xNiO_3$ perovskite-type oxide catalysts were prepared using a one-step, sol−gel synthesis method, with citric acid serving as the complexing agent.[12,48,49] The gram quantities of the precursors used to synthesize the materials are summarized in Table 1, where the metal ratio of $Ce_{1-x}Co_x$ was varied to subtitute the A-site (Ce) in $CeNiO_3$. Here x represents the mass (g) of Co precursor (x = 0.25, 0.50, 0.75). It should be noted that the mass of nickel precursor and citric acid were kept constant at 1.75 and 2.75 g, respectively, throughout the catalyst synthesis process.[12] For simplicity, the synthesized catalysts with the following $Ce_{1-x}Co_x$ ratios of $Ce_{0.75}Co_{0.25}$, $Ce_{0.50}Co_{0.50}$, and $Ce_{0.25}Co_{0.75}$ were labeled as CCN-1, CCN-2, and CCN-3, respectively, as noted in Table 1. To formulate the materials, the desired amounts of metal precursors and citric acid were mixed in 50 mL of DI water. The solution was stirred at 450 rpm at 150 °C until a viscous gel was formed, a process that took approximately 50−60 min. Once a gel-like solution was obtained, it was transferred to a convection oven and dried at 120 °C for 12 h. The powder was then ground with a mortar and pestle and calcined in air at 720 °C (ramp of 10 °C/min) for 5 h. The resulting powder was cooled to room temperature and again ground to make a homogeneous powder, and then it was sieved through a 0.135 mm mesh.

2.3. Structured BFM Monoliths Formulation

The sieved catalyst powders were converted into printable inks using the ratios reported in Table 2 and 3D-printed into BFM honeycomb monoliths using the processes outlined in our earlier works.[50−53] Briefly, the sieved catalyst powders were mixed with $CaCO_3$, bentonite, and methylcellulose using ∼20 mL of DI as a suspension solvent. The ink was sonicated for 30 min after combining all components and was allowed to roll at 60 rpm for 48 h (T = 25 °C) to achieve homogeneity and generate binding. The obtained slurry was then densified at 50 °C under immersion mixing at 600 rpm until a printable rheology was achieved. A printable rheology is defined here as being shear thinning, self-standing, and retaining its solvent. The inks were printed using our established hydraulic printing setup,[52] dried at 25 °C in the fume hood for 12 h to prevent cracking, and finally calcined in air at 700 °C (ramp = 10 °C/min) for 5 h. The BFM monoliths were denoted as CCN-1/Ca, CCN-2/Ca, and CCN-3/Ca, where Ca represents the adsorbent phase CaO. An example of one of the printed honeycombs is shown in Figure 1. As evident, this process generated an open cell structure with ∼200 cells per square inch (cpsi) cell density and ∼1 cm outer diameter.

Table 2. Paste Composition of 3D-Printed-Structured BFM Monoliths

BFM monolith	catalyst (wt %)	adsorbent (wt %)	bentonite (wt %)	methylcellulose (wt %)
CCN-1/Ca	45	45	7	3
CCN-2/Ca	45	45	7	3
CCN-3/Ca	45	45	7	3

2.4. Structured BFM Monoliths Characterization

The textural properties of the monoliths were assessed by using N_2 physisorption on a Micromeritics (3Flex) gas analyzer at 77 K. The samples were degassed at 350 °C for 6 h on a Micromeritics Smart VacPrep instrument before analysis. The pore size distribution (PSD) and surface area were approximated from the N_2 physisorption isotherms via the nonlocal density functional theory (NLDFT) and Brunauer−Emmett−Teller (BET) methods, respectively. The elemental dispersions of the various metal oxides and the surface topography were assessed via field emission scanning electron microscopy (FE-SEM; Quanta 600F ESEM) with a Bruker Quantax energy-dispersive spectrometer (EDS). The oxidation states were evaluated via X-ray photoelectron spectroscopy (XPS) on a Thermo Scientific Nexsa 128 channel XPS system. The scan conditions for each component are summarized in Table S1 of the Supporting Information.

The crystallinities of the synthesized catalysts and ground honeycombs were assessed via a PANalytical X'Pert multipurpose X-ray diffractometer with a scan step size of 0.026°/step at a rate of 3°/min from 5° ≤ 2θ ≤ 90°. The reducibility of the materials was assessed on 3Flex via temperature-programmed reduction in hydrogen (H_2-TPR), whereas the catalytic acidities were assessed via temperature-programmed desorption of ammonia (NH_3-TPD). Both processes were carried out on 3Flex using the pretreatment and ramp conditions outlined in our earlier work,[11] and the catalytic acidic densities were calculated following a method reported in our prior works.[54,55]

2.5. *In Situ* XRD Measurements

To better understand the changes in the chemical structure of BFM materials during CO_2 adsorption−desorption at high temperatures, *in situ* X-ray diffraction (XRD) analysis was conducted on a PANalytical X'Pert multipurpose XRD with a scan step size of 0.026°/step at a rate of 13°/min from 5° ≤ 2θ ≤ 70°. Prior to runs, the samples were heated to 700 °C at a rate of 10 °C/min under 200 mL/min of N_2. After isothermal treatment for 1 h, the system was cooled under N_2 until it reached 600 °C, at which point the gaseous feed was changed to 200 mL/min of CO_2. Adsorption was allowed to progress for 60 min, where XRD scans were recorded every 5 min. The desorption behavior was then subsequently collected. In this step, the feed was changed back to 200 mL/min of N_2 and the system was heated at 10 °C/min to the target temperatures of 600, 650, or 700 °C. It should be noted here that the adsorption temperature was held constant across runs, but the desorption temperature was varied to assess the effect of thermal activation on BFM crystallinity. A fresh sample was used in each run to avoid any discrepancy, which may have occurred in the crystallinity as a result of sample recycling.

2.6. *In Situ* CO_2 Capture and Utilization Experiments

The combined CO_2 capture-conversion experiments were performed using the system detailed in our prior work.[11] The effluent concentration profiles for all components were monitored and recorded using a MKS II mass spectrometer, and the product distribution was assessed using correlations detailed in our prior works and reported in the Supporting Information, eqs S1−S7.[35,36] In a typical experiment, 0.5 g of BFM was placed in the middle of a stainless-steel reactor with dimensions of l.14 cm inner diameter and 22.8 cm height. The BFM was packed into two layers of quartz wool

https://doi.org/10.1021/jacsau.3c00553
JACS Au 2024, 4, 101−115

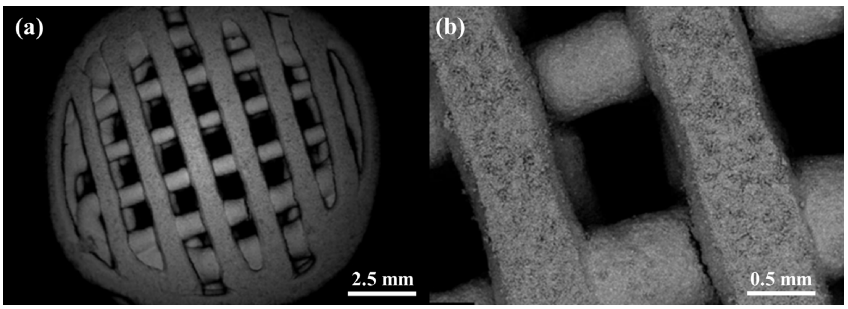

Figure 1. SEM micrographs of (a) the top view of the BFM monolith and (b) corresponding channel dimensions.

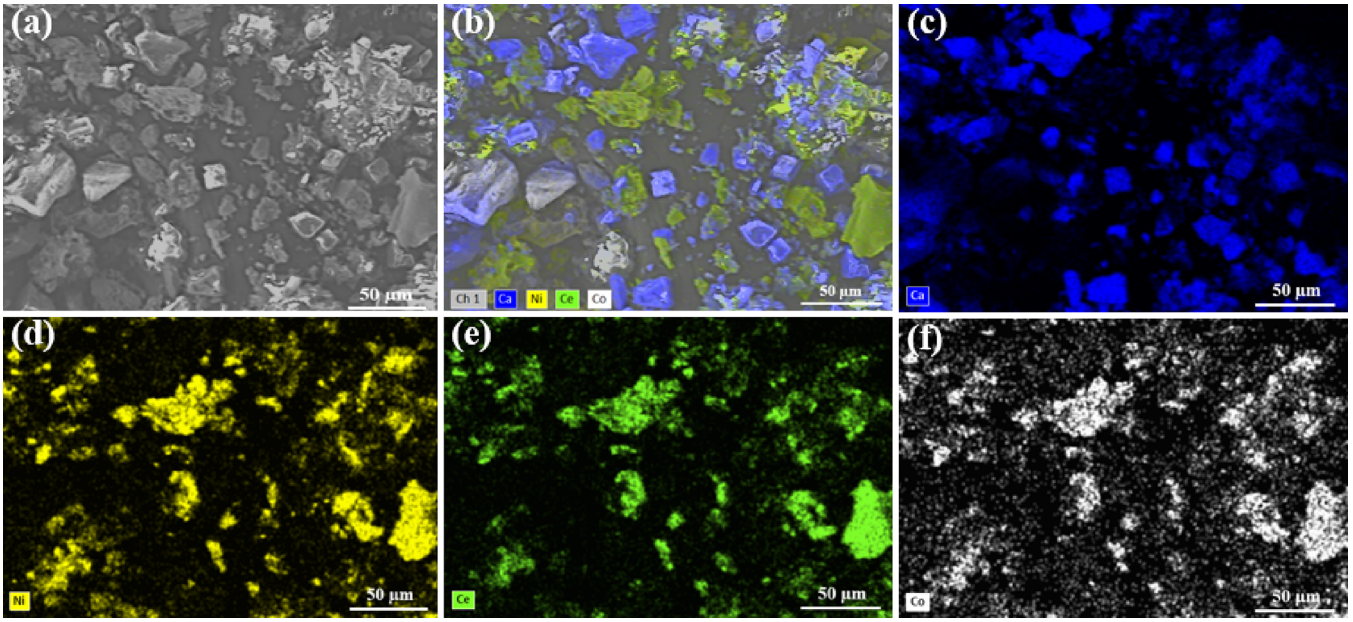

Figure 2. (a) SEM and (b–f) EDS mapping images of the CCN-1/Ca BFM monolith (fresh sample).

to prevent gas bypass. The samples were first pretreated by heating at 10 °C/min to 700 °C for 1 h under 30 mL/min flow rate of Ar. The bed was cooled to the adsorption temperature (600 °C), wherein 25 mL/min of 10% CO_2/Ar was flown into the reactor until saturation of CO_2 concentration was observed. After the CO_2 concentration plateaued, the flow of 10% CO_2/Ar was terminated, and a 25 mL/min flow of CH_4/Ar was flowed into the system. The bed was then heated or cooled at a rate of 100 °C/min to the target temperature, which varied across experiments from 500, 600, 650, and 700 °C. The reaction was then allowed to progress until the effluent CO_2 reached zero. A Q500 thermalgravimetric analyzer (TGA) from TA Instruments was used for coke formation analysis after the adsorption-reaction experiments. Therein, the surface of spent samples was heated through flowing 40 mL/min of N_2 at 900 °C using a 25 °C/min ramp. The coke species were then identified using a combination of Raman spectrometry on a μ-Raman spectrometer (ARAMIS; HORIBA Jobin Yvon Inc., Edison, NJ) using an He–Ne laser (632.8 nm) as well as by traditional Fourier transform infrared (FTIR) spectrometry using a Nicolet Nexus 470 spectrometer. The two characterizations showed similar functional groups, so only the conventional FTIR is included in the main body.

3. RESULTS AND DISCUSSION

3.1. Characterization of BFM Monoliths

The sample morphologies and elemental dispersions were assessed with a combination of SEM and EDS. The topographies and elemental dispersions for CCN-2/Ca and CCN-3/Ca were nearly identical to those shown in Figure 2, so they are contained in Figures S1 and S2, Supporting Information. Looking at the elemental dispersions, it was observed that all four components—namely, Ca (Figure 2c), Ni (Figure 2d), Ce (Figure 2e), and Co (Figure 2f)—were all uniformly dispersed throughout the backbone of the material. Given that these dispersions were consistent in the other samples, it was first concluded that changing the cobalt concentration did not substantially influence the other metallic dispersions, as shown in Figure 2d–f. These findings indicate that metallic components were successfully incorporated into the catalyst phases. However, mixing the adsorbent (CaO) with the catalyst resulted in a combination of segregated and direct contacts between the adsorbent and catalyst phases. This arrangement, especially the direct contact between phases, enabled the developed BFMs to function in a truly bifunctional manner. The performance of catalytic materials largely depends on maintaining effective contact between the metal components. Similarly, the efficacy of BFMs is contingent upon the degree of mixing between the adsorbent and catalyst phases. The presence of direct contact between the adsorptive and catalytic phases, which is crucial for the effectiveness of these BFMs, is evident here. Figure 2 supports this, suggesting that the materials are likely to act as bifunctional materials despite some segregation between phases. The presence of direct contact between the adsorbent and catalyst is key to the rapid migration of CO_2 from the adsorbent to the catalyst

https://doi.org/10.1021/jacsau.3c00553
JACS Au 2024, 4, 101–115

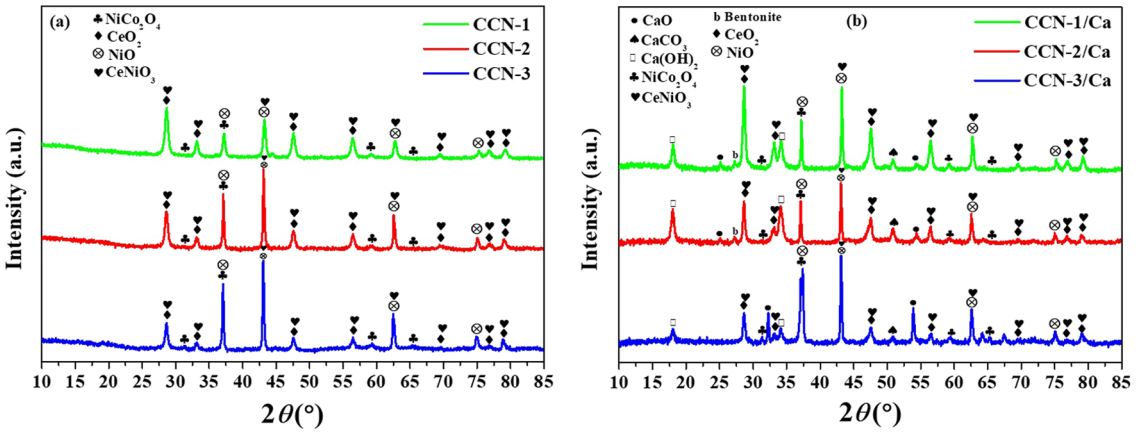

Figure 3. XRD analysis of (a) bare catalysts and (b) BFM monoliths.

during the desorption step, which is essential for an efficient CO_2 reaction.

Figure 3a,b display the crystallinities of the pristine catalysts and 3D-printed monoliths, respectively. The Rietveld Refinement (RIR) quantitative analysis is also provided for CCN-3/Ca in Figure S3 for reference. Examining the pristine catalysts first, a series of diffraction peaks were observed at 2θ = 28.7°, 33.1°, 43.2°, 47.4°, 56.3°, 62.8°, 69.41°, 76.6°, and 79.1°, which corresponded the crystal planes of (111), (002), (221), (040), (321), (331), (242), (412), and (161) in $CeNiO_3$ perovskite, respectively. Although the perovskite phase of $CeNiO_3$ was not explicitly identified by the RIR, possibly due to overlapping reflections, the observed diffraction peaks matched those reported in the literature for $CeNiO_3$, suggesting the presence of the perovskite phase.[77] Additionally, several diffractive peaks were observed for CeO_2 at 2θ = 28.56°, 33.08°, 47.47°, 56.3°, 69.40°, 76.6°, and 79.07°, corresponding to the crystal planes of (111), (200), (220), (311), (400), (331), and (420), respectively.[56] Diffractive peaks for NiO were observed at 2θ = 37.1°, 43.1°, and 62.4°, which corresponded to the (111), (200), and (220) planes, respectively.[57,58] Finally, the peaks appeared at 2θ of 31.1°, 36.6°, 59°, and 65.1° were correlated to the crystal planes of (220), (311), (511), and (440) in $NiCo_2O_4$ (nickel cobaltite), respectively.[59,60] From Figure 3a, it can be deduced that substituting the A-site in $CeNiO_3$ with various $Ce_{1-x}Co_x$ ratios resulted in the formation of different phases alongside the $CeNiO_3$ perovskite, namely $NiCo_2O_4$, NiO, and CeO_2 metal oxides.

After the printing process, new diffraction peaks emerged at 2θ = 32.1°, 37.1°, and 53.9° for CaO[61] and 2θ = 18.1° and 33.8° for $Ca(OH)_2$. Other minor peaks detected at 2θ = 27.1° and 50.8°, were attributed to bentonite clay and $CaCO_3$, respectively.[62−64] Importantly, the 3D printing process did not alter the crystallinity of the formed phases, as evidenced by the consistent diffraction patterns observed in Figure 3b. From these observations, we can reasonably conclude that the BFMs were mainly mixed-metal oxides comprising $CeNiO_3$ perovskite, $NiCo_2O_4$, NiO, CeO_2, and CaO, with a few residuals resulting from the synthesis process.

Moreover, the crystalline structures remained consistent across different Ce_{1-x}/Co_x ratios. Nevertheless, the peak at 2θ = 28.2° for CeO_2 was more pronounced in the $Ce_{0.75}Co_{0.25}$ ratio compared to other ratios, which can be attributed to the increased content of Ce. Similarly, the peak at 2θ = 36.6° was more prominent in $Ce_{0.25}Co_{0.75}$, due to the increased Co content. The minor peaks at 2θ = 31.5° and 65.1° were observed in $Ce_{0.25}Co_{0.75}$ but were barely noticeable/or disappeared in $Ce_{0.50}Co_{0.50}$ and $Ce_{0.75}Co_{0.25}$, due to the lower Co content. In summary, the XRD results suggested that the 3D printing process had a minimal impact on the crystallinity of the catalyst and any significant changes in catalytic activity are likely to be primarily driven by redox properties and reactive oxygen species, resulting from the varying $Ce_{1-x}Co_x$ ratios, rather than by alterations in the crystalline structure.

The N_2 physisorption isotherms and PSD profiles of the BFMs are shown in Figure S4a,b, respectively, and the corresponding textural properties are provided in Table S2. Looking first at the adsorption isotherms, the samples all displayed Type II hybridized with type IV isotherms corresponding to nonporous behavior, albeit with some mesoporosity behavior as defined by the IUPAC classification.[65] Indeed, the PSD profiles corroborate the mesoporosity of the materials, as the pores all existed between 3 and 10 nm, except for a narrow pore size of less than 2.5 nm. However, it should be noted that the pore volumes for all three BFMs were low overall. The mesoporosity shown in Figure S4b can be attributed to the adsorbent and binder precursors used during the synthesis of the materials. These results were not all that surprising, given that metal oxide catalysts and CaO possess low porosity, aside from a few specific instances with higher surface area.[66,67] This conclusion is further supported by the textural properties in Table S2, where it was observed that all three monoliths had virtually identical pore volumes and surface areas. It should further be noted that the $Ce_{1-x}Co_x$ ratio again had no influence on the properties of the BFMs, as the changes in the surface area and pore volume were within the confines of accepted instrumental error. This behavior agreed with the XRD patterns in Figure 3 as well as by the elemental dispersions in Figure 2 and Figures S1 and S2, Supporting Information, which both indicated that the metallic fractions had minimal influence on the characteristic properties of the BFMs. Therefore, the differences in material activity for combined CO_2 capture and utilization in DMR were further anticipated to be heavily driven by changes in coke formation behavior and redox properties, rather than by any deviations in crystallinity, textural properties, or elemental dispersion.

3.2. Acidity and Redox Properties of 3D-Printed BFMs

The catalytic acidities of both the bare catalysts and the 3D-printed BFM monoliths were assessed using NH_3-TPD, with

https://doi.org/10.1021/jacsau.3c00553
JACS Au 2024, 4, 101−115

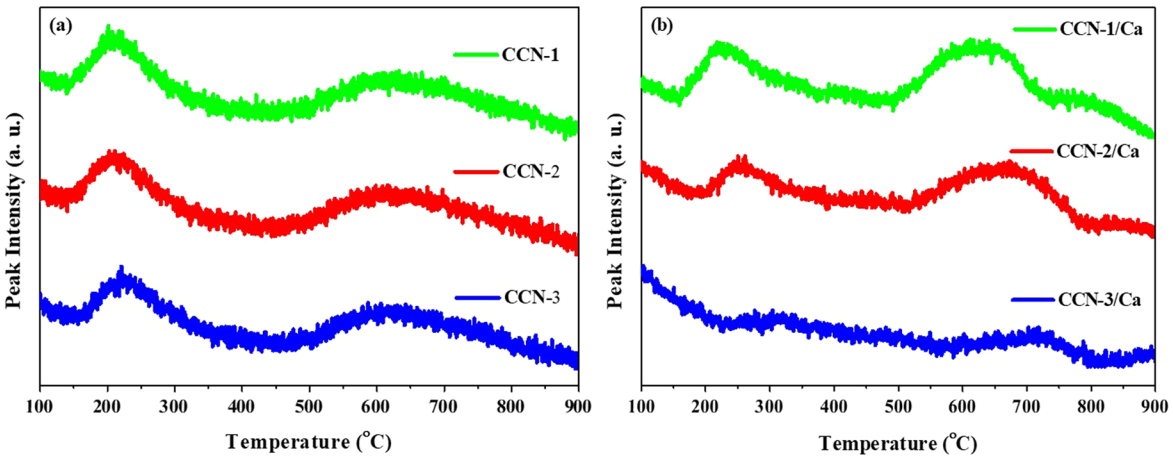

Figure 4. NH_3-TPD profiles of (a) bare catalysts and (b) BFM monoliths.

results depicted in Figure 4 and quantified acidities summarized in Table 3. Initial observations of the bare catalysts (Figure 4a) revealed desorption peaks at T = 225 and 500−800 °C, corresponding to weak and strong acid sites, respectively. Notably, the intensity of these peaks was not influenced by the cobalt content, implying that cobalt loading has a little effect on catalytic acidity. Nevertheless, as Table 3 indicates, the quantity of acid sites correlates directly with the $Ce_{1-x}Co_x$ ratio; acidity decreases in the order of CCN-1/Ca > CCN-2/Ca > CCN-3/Ca. Given that metal oxides do not neatly fit into the conventional Lewis/Brønsted acidic-basic site concepts, as is the case with other materials like zeolites that have well-defined structures and typically contain only one or two types of metal ions, these findings suggest a more complex surface chemistry. The observed acidic behavior in this case might be attributable to defects, oxygen vacancies, metal ion states, and the interactions among Ce, Ni, and Co cations in the mixed oxide structure. While cerium is generally more acidic than cobalt, this results in an increased acid density overall, but within a similar temperature range. Such complexity could enhance the adsorption and activation of oxygen-containing species during redox reactions.[68,69]

Table 3. Acid Site Quantification of Catalysts and 3D-Printed BFM Monoliths from NH_3-TPD

sample	weak acid sites (mmol NH_3/g_{cat})	strong acid sites (mmol NH_3/g_{cat})	total acid sites (mmol NH_3/g_{cat})
CCN-1	0.20	0.21	0.41
CCN-2	0.18	0.19	0.37
CCN-3	0.15	0.16	0.30
CCN-1/Ca	0.14	0.18	0.32
CCN-2/Ca	0.13	0.14	0.27
CCN-3/Ca	0.07	0.08	0.15

Concerning the acidity of the 3D-printed monoliths, several key observations were made. First, similar ammonia desorption temperatures, as shown in Figure 4b, suggest that the bonding strength of the acid sites remained unaffected by the 3D printing process. Moreover, the ratio of strong to weak acid sites in these monoliths closely mirrored that found in the as-synthesized catalyst powders, maintaining an approximate 1:1 ratio between weak and strong acid sites. However, the overall number of acid sites did decrease postprinting, a predictable outcome given that neither CaO nor bentonite clay possesses acidic properties. Therefore, dilution of the catalyst phases with the nonacidic binder and adsorbent material naturally led to a reduction in total acidity per unit weight. From these observations, two significant conclusions can be drawn: (i) the catalytic acidity is directly proportional to the $Ce_{1-x}Co_x$ ratio

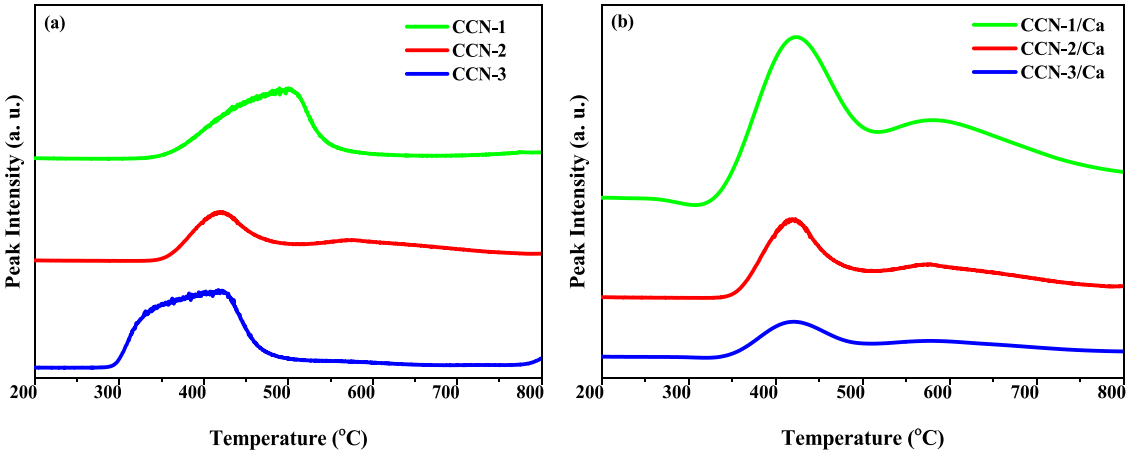

Figure 5. H_2-TPR profiles of (a) as-synthesized catalysts and (b) BFM monoliths.

https://doi.org/10.1021/jacsau.3c00553
JACS Au 2024, 4, 101−115

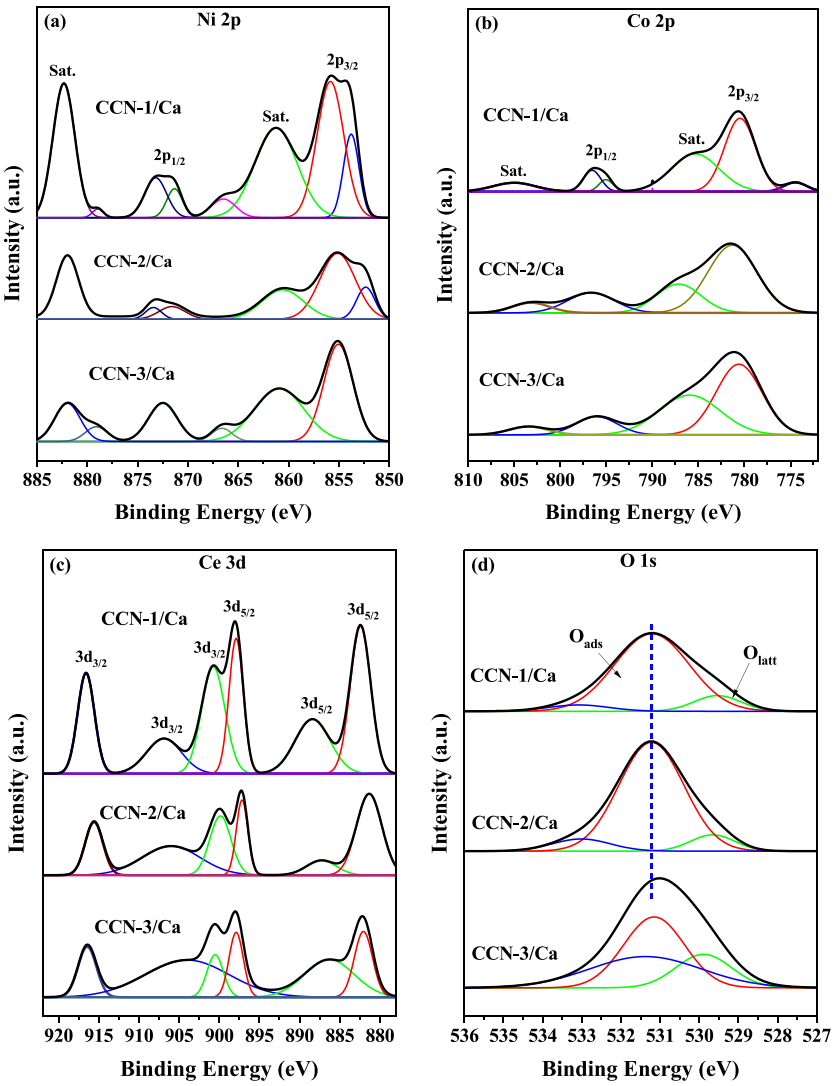

Figure 6. High-resolution XPS spectra of structured BFM monoliths (a) Ni 2p, (b) Co 2p, (c) Ce 3d, and (d) O 1s.

with expected higher reducibility due to complex surface chemistry attributable to defects, metal ion states, and the interactions among metal cations, and (ii) the 3D printing process itself does not alter the intrinsic acidity of the catalyst, except for the anticipated decrease resulting from dilution with the binder and adsorbent. Considering that the performance in DMR process is largely dictated by the reducibility of the catalysts and the availability of active surface oxygen species,[70−72] the samples with a $Ce_{0.75}Co_{0.25}$ ratio are expected to deliver optimal capture and conversion efficiency due to their anticipated high reducibility.

To assess the influence of the $Ce_{1-x}Co_x$ ratio on reducibility, the redox properties of the materials were evaluated using H_2-TPR in the temperature range of 200−800 °C, as shown in Figure 5. In the pristine catalysts (Figure 5a), a singular, broad peak was observed between 300 and 550 °C. This peak, resulting from the overlap of reductions from chemisorbed oxygen species and interactive metal species, shifted to higher temperatures with increasing cerium concentrations. These H_2-TPR results confirm the complexity of the surface chemistry, as evidenced by this broad peak.[26] The reduction peak in the catalysts is primarily due to the reduction of oxygen species chemisorbed onto oxygen vacancies. Co and Ni species tend to reduce at lower temperature compared to Ce species, as indicated by the shift of the reduction peak to a higher temperature in $Ce_{0.75}Co_{0.25}$. This notation is in agreement with the literature,[26,73,74] where it has been observed that ceria species typically cause reductions to occur at higher temperatures compared to cobalt and nickel. Therefore, we can reasonably conclude that the reduction of cobalt and nickel in the $NiCo_2O_4$ and NiO phases occurs at lower temperatures than that of cerium in CeO_2, and the overall reduction process is influenced by the chemisorbed oxygen species resulting from the interactive species of Co, Ni, and Ce.

In Figure 5b, the reduction temperature remained roughly consistent across all three $Ce_{1-x}Co_x$ ratios with slight shift in the temperature range for the broad reduction peak and emergence of a peak at higher temperature (~600 °C). This behavior could be attributed to variations in reducibility, resulting from the addition of binder and adsorbent, which might lead to segregated reductions of metal species at 600 °C. This is likely the case for Ce species, as was clearly observed in the $Ce_{0.75}Co_{0.25}$ ratio. Therefore, when correlating Figure 5 with prior characterizations, it appears that BFM's catalytic performance would be primarily influenced by changes in redox properties and secondarily by acidic features. Given that

https://doi.org/10.1021/jacsau.3c00553
JACS Au 2024, 4, 101−115

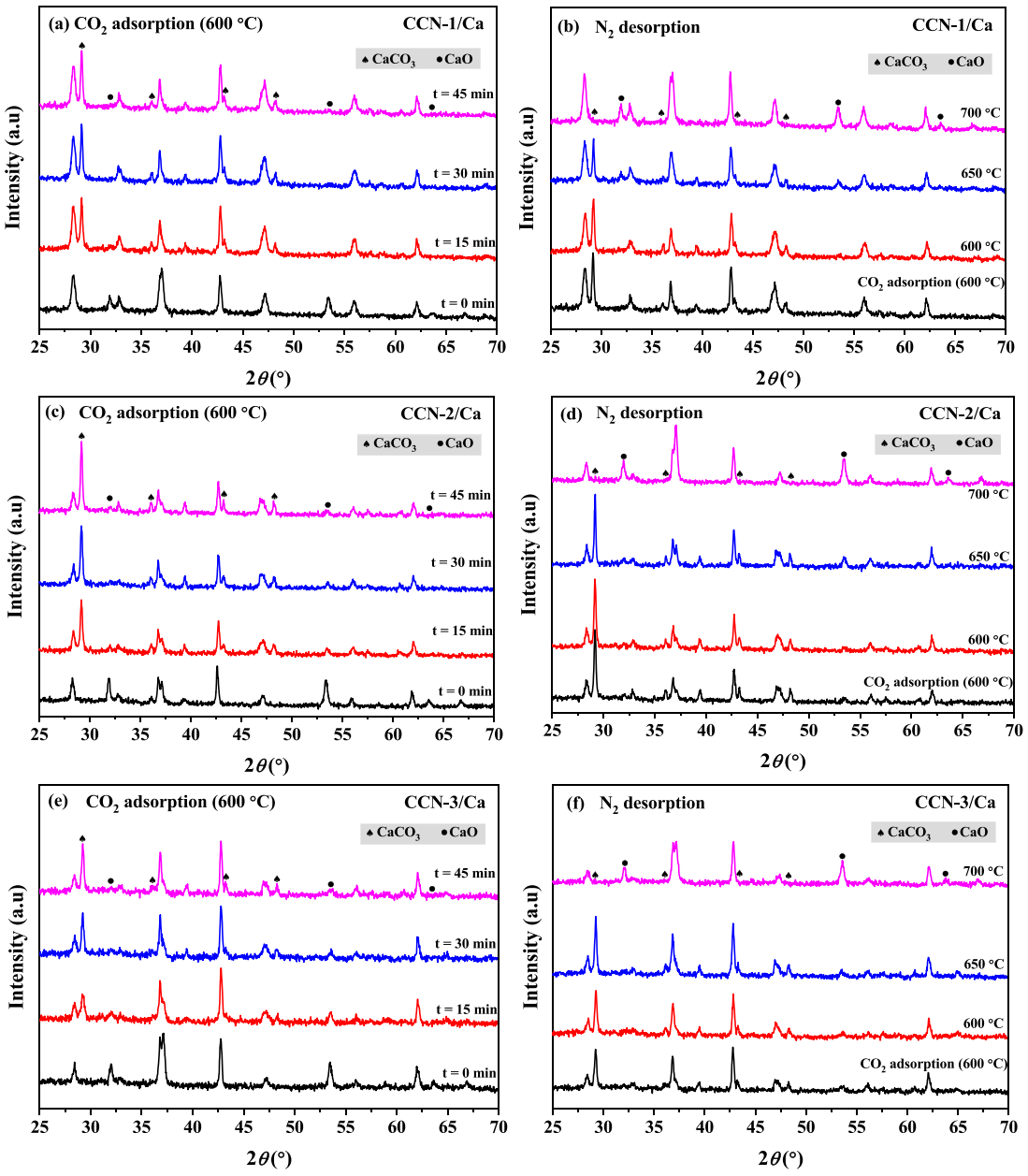

Figure 7. *In situ* XRD spectra for CO_2 adsorption (left) and desorption (right) of (a, b) CCN-1/Ca, (c, d) CCN-2/Ca, and (e, f) CCN-3/Ca BFM monoliths.

methane reforming reactions occur at higher temperatures, above 500 °C, the best overall performance is anticipated for the CCN-1/Ca BFMs, owing to their enhanced reducibility at elevated temperatures.

The XPS analysis was conducted to determine the influence of $Ce_{1-x}Co_x$ ratio on the orbital spins of the BFMs, as depicted in Figure 6. For the Ni 2p orbital (Figure 6a), peaks corresponding to Ni $2p_{3/2}$ at 854.9 eV and Ni $2p_{1/2}$ at 872.6 eV were identified. Additionally, two satellite peaks at 861.2 and 882.3 eV suggest the presence of Ni^{2+} and Ni^{3+} species, respectively.[21,75] Turning to the cerium spectra (Figure 6c), we observed spikes that correspond to the binding energies of Ce^{3+} $3d_{3/2}$ and Ce^{4+} $3d_{5/2}$, along with satellite signals. Specifically, Ce^{3+} showed binding energies at 916.6, 907.1, and 900.7 eV, while Ce^{4+} had binding energies at 897.9, 888.3, and 882.4 eV.[74,76,77] Next, the cobalt spectra (Figure 6b) featured peaks at 796.1 eV (Co $2p_{1/2}$) and 780.6 eV (Co $2p_{3/2}$), which were attributed to Co^{3+} and Co^{2+}, respectively.[76] Importantly, the intensity and number of deconvoluted peaks in the Ni 2p orbital increased upon increasing $Ce_{1-x}Co_x$ ratio. Such effects suggest that increasing the cobalt content negatively impacts the catalyst's electron structure, particularly in dry reforming processes where nickel species are instrumental in facilitating the breaking of C−H bonds. This agrees with prior work by Liang et al., who found that electron-rich Ni sites enhance CH_4 conversion in DMR process.[78]

The $Ce_{1-x}Co_x$ ratio also significantly influenced the ceria (Figure 6c) and oxygen (Figure 6d) spectra. For instance, a $Ce_{0.75}Co_{0.25}$ ratio resulted in more intense peaks in the Ce 3d orbital (890−920 eV), implying a likely decrease in methane reforming behavior with reduced Ce 3d orbital intensity, given that ceria imparts active surface oxygen.[71,79] Similarly, increasing the cobalt concentration led to a shift toward lower binding energies for oxygen orbitals, which are known to

https://doi.org/10.1021/jacsau.3c00553
JACS Au 2024, 4, 101−115

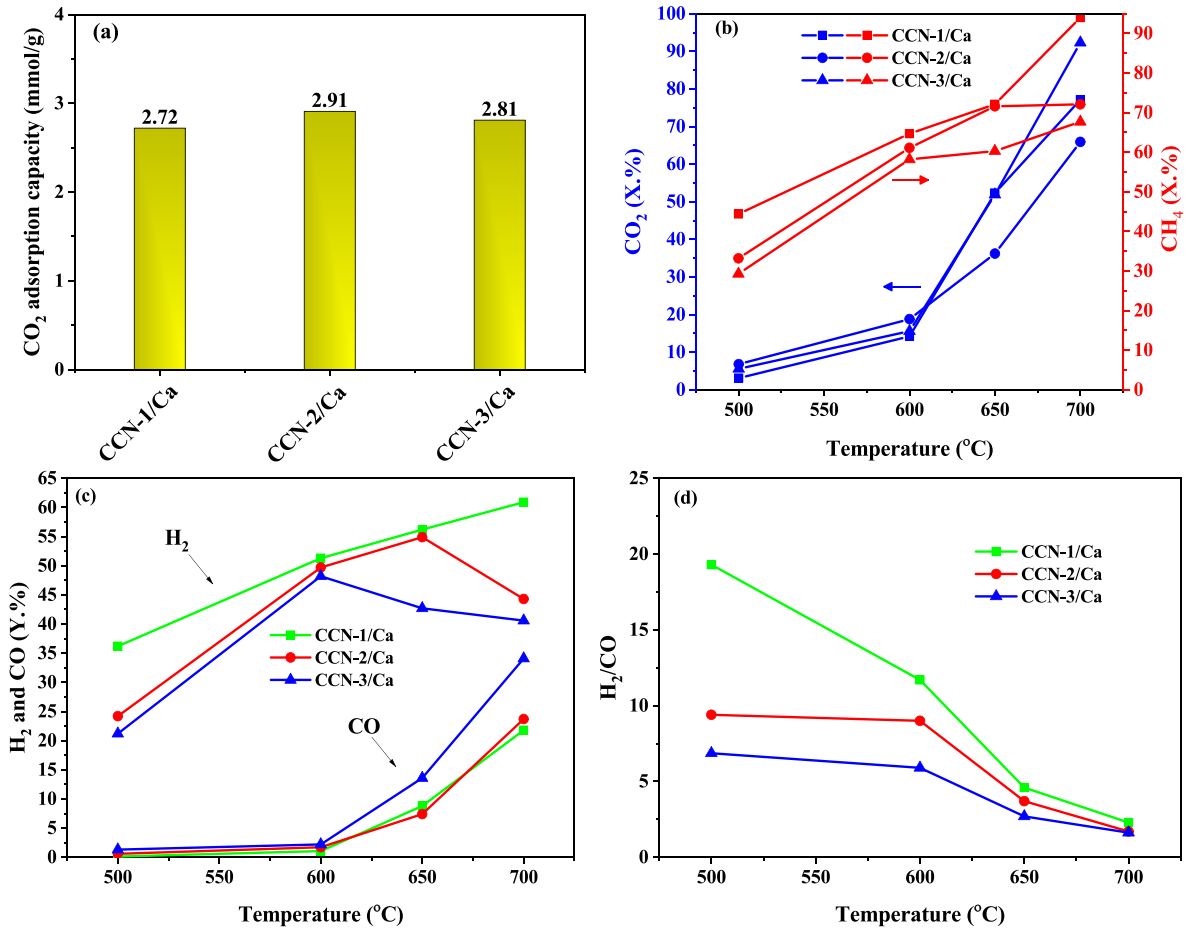

Figure 8. (a) TGA CO_2 adsorption capacities at 600 °C as well as corresponding (b) CO_2 and CH_4 conversions, (c) H_2 and CO yields, and (d) H_2/CO ratio with an adsorption temperature of 600 °C and reaction temperatures from 500 to 700 °C for 3D-printed BFM monoliths.

play a significant role in the methane reforming product distribution. It can be reasonably induced that Ce increases the number of oxygen vacancies on the surface of the catalyst. This is because Ce has a higher oxidation state than Co; therefore, it can donate electrons to the material. These electrons can create oxygen vacancies by reducing lattice oxygen ions to oxygen atoms, as evidenced on the reduced binding energy of O_{latt}. The increased number of oxygen vacancies provides more sites for oxygen adsorption, which leads to an increase in the O_{ads}/O_{latt} ratio. Co, on the other hand, could promote the formation of surface Co−O bonds. This is because Co has a strong affinity for oxygen, which can form Co−O bonds with oxygen atoms on the surface. These Co−O bonds compete with oxygen adsorption sites, which leads to a decrease in the amount of adsorbed oxygen on the surface of the catalyst. This, in turn, leads to a decrease in the O_{ads}/O_{latt} ratio.[80]

A peak at 533.10 eV indicates the presence of carbonates (ca. CO_3^{2-}),[81] likely residual from $CaCO_3$ during synthesis of BFMs. The presence of these carbonates was confirmed by C s1 shown in Figure 5S. The high-resolution C 1s spectra, presented in Figure 5S, reveal two distinct peaks with binding energies at 284.4 and 289.3 eV. The peak at 284.4 eV is associated with carbons originating from the instrumentation, while the peak at 289.3 eV is indicative of carbonate species (ca. CO_3^{2-}). Given these insights, it can be inferred that the BFMs still retain carbon species after synthesis.

3.3. *In Situ* XRD Assessment of CO_2 Adsorption/Desorption

The effect of adsorption/desorption conditions on BFM crystallinity was assessed via *in situ* XRD across the various compositions, as shown in Figure 7. First looking at the changes in crystallinity during adsorption, it should be noted that several new peaks appeared at 2θ = 29°, 36°, 43°, and 48° within 15 min in CCN-1/Ca (Figure 7a), CCN-2/Ca (Figure 7c), and CCN-1/Ca (Figure 7e), respectively, which signifies the formation of $CaCO_3$.[61,66] Such effects indicated that the $Ce_{1-x}Co_x$ ratio did not detrimentally affect the crystalline structure, but it did influence the ability of the BFMs to tether CO_2 addition onto CaO through changing the required energy for CO_2 and CaO interactions. However, it should also be noted that the CCN-3/Ca sample did show a complete loss of its plane at 2θ = 32.4°, whereas the other samples all retained the secondary index to some degree. Given that this peak corresponds to the (111) plane in CaO, its complete obstruction in CCN-3/Ca signified that the sample had a lower thermal barrier to form $CaCO_3$ (2θ = 29°). Such higher thermodynamic favorability should cause the adsorption to be less reversible.[82] Indeed, the diffractive indices during desorption confirmed this behavior, as CCN-3/Ca only reformed the CaO crystalline plane at T = 700 °C (Figure 7f), whereas CCN-2/Ca and CCN-1/Ca exhibited stronger peak reformation of 2θ = 32.4° at 650 °C (Figure 7b,d). This lower temperature regeneration—which, again, is associated with weaker CaO and CO_2 complexing—could be reasonably

https://doi.org/10.1021/jacsau.3c00553
JACS Au 2024, 4, 101−115

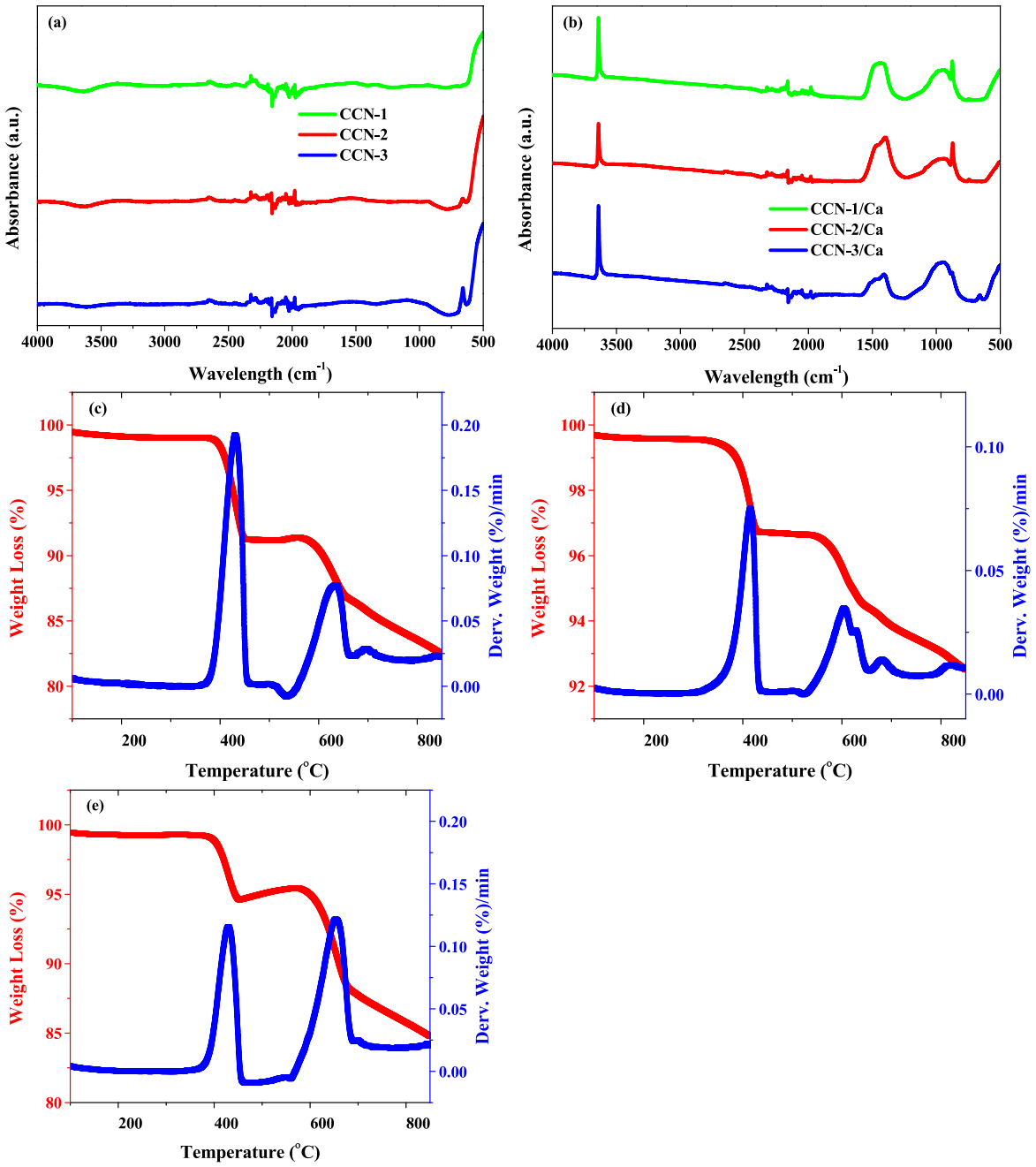

Figure 9. FTIR analysis of (a) bare catalysts and (b) BFM monoliths as well as TGA profiles of (c) CCN-1/Ca, (d) CCN-2/Ca, and (e) CCN-3/Ca samples.

expected to allow CO_2 to be more readily accessible during the reaction step, thus enhancing its conversion and providing a more favorable pathway toward utilization. As such, Figure 7 likely indicated that the best overall BFM performance would be observed in the CCN-1/Ca sample, which was in line with its assessment of chemical properties and was confirmed by the adsorption/reaction experiments in the next section.

3.4. Direct Synthesis of H_2 from CO_2 and CH_4 over Structured BFM Monoliths

The synthesized structured BFM monoliths were assessed for combined CO_2 capture and conversion via the CO_2-DMR reaction at an isothermal adsorption-reaction temperature of 600 °C. The adsorption/reaction profiles and performances of the as-synthesized catalysts are shown in Figure S6, Supporting Information for reference. Looking first at the measured CO_2 adsorption capacities (Figure 8a), the quantity of CO_2 adsorbed was within an acceptable error margin across the three structured BFMs (2.72−2.91 mmol/g), indicating that the composition of the catalyst phase did not generate any synergistic attraction between CO_2 and CaO. As such, the CO_2 adsorption capacity was not considered to be a limiting factor for catalyst performance given its similarity across the three BFMs. Differences in catalytic performance can be attributed to variations in the chemical properties of the catalysts. Specifically, two key factors were identified: first, the reducibility of the catalyst, as illustrated in Figure 5b; and second, the facility of surface electron transfers, which is influenced by the availability of different oxygen species

https://doi.org/10.1021/jacsau.3c00553
JACS Au 2024, 4, 101−115

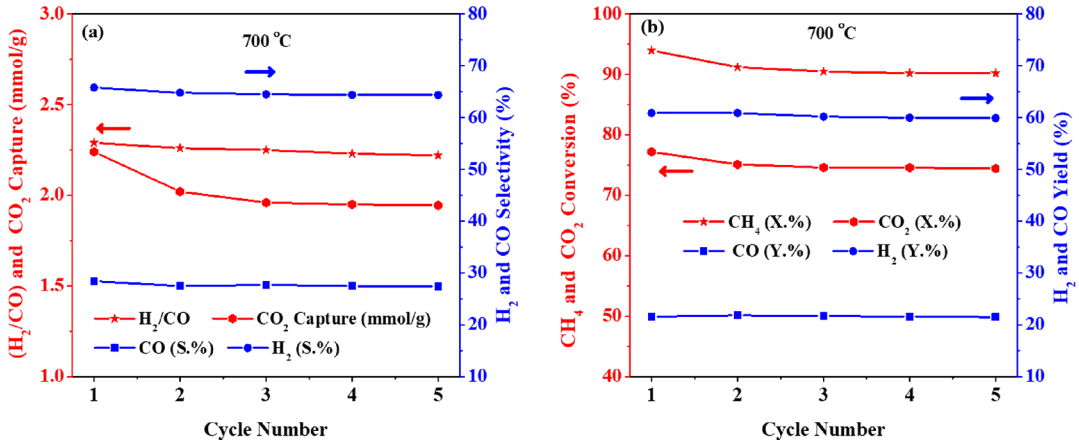

Figure 10. (a, b) Cyclic experiments (adsorption-reaction) of the CCN-1/Ca monolith at 600−700 °C.

(Figure 6d). These characteristics are crucial for enhancing the efficiency of redox reactions during the reaction process. On this basis, the degrees of CO_2 and CH_4 conversion (Figure 8b) as a function of temperature and catalyst composition were considered as the first metric of performance. It was evident that the conversion of both reactants rose with the ceria loading regardless of the temperature, thus cementing that the reducibility and oxygen availability drive dry methane reforming across the BFMs. On the other hand, it should be noted that both CO_2 and CH_4 conversions were increased as a function of temperature. Considering the known reaction mechanisms (eqs S9−S13) these behaviors were taken to signify a thermodynamic shift toward H_2 synthesis from CH_4 mainly by reforming and cracking reactions. This behavior was reflected by the H_2/CO ratio (Figure 8d) in all three samples; however, the H_2 yield continued to increase for CCN-1/Ca above the 600 °C threshold. The latter effect seems to be a unique property of the CCN-1/Ca BFM, likely being caused by its high catalytic reducibility and lower binding strength with CO_2, since these aspects of the BFM are known to drive H_2 production from CH_4 reforming.[12] However, the higher H_2/CO ratio and lower CO_2 conversion at 500 °C, as shown in Figure 8d, could suggest greater CO_2 retention within the adsorbent phase or a less favorable conversion of CO_2 to CO via the reverse water−gas shift (RWGS) and DMR reactions (eqs S9 and S12).[46] These reactions are generally more prominent at higher temperatures. If that is the case, the methane cracking pathway (eq S12) leading to direct hydrogen production might be the primary contributor to the observed H_2 levels, particularly in CCN-1/Ca. However, as discussed in the subsequent section on carbon analysis, coke formation was minimal. This trend is likely related to the availability of reactive oxygen species, which are known to enhance catalyst activity at lower energy thresholds, thereby promoting CH_4 reforming and increasing H_2 yield.[12,72,83,84] In summary, our study highlights the exceptional performance of CCN-1/Ca, particularly at an optimal temperature of 700 °C. This bifunctional material outperforms its counterparts in the existing literature,[21,23,85] as evidenced by the data presented in Figure 8. Our results thus present a promising approach for manufacturing mixed metal oxide BFMs, specifically for applications in CO_2 capture and H_2 production.

The surface vibrational modes of the catalysts were assessed before and after the reaction through FTIR, as illustrated in Figure 9. Distinct vibrational modes were observed after reaction at wavelengths of 1500 and 980 cm^{-1} in all three samples, irrespective of the $Ce_{1-x}Co_x$ ratio. These bands are associated with the formation of various carbonates on the surface of the catalysts. To further investigate this, TGA experiments were conducted on fresh BFM samples, and the results are presented in Figure S7a−c. Peaks appearing between 600 and 800 °C can be attributed to the release of carbon species during sample annealing. These peaks also suggest coke formation if spent samples are analyzed. Thus, this observation supports the previous notion that BFMs were not fully regenerated from carbonates during their synthesis. This conclusion is consistent with the XRD results that showed residual calcium carbonates, and the XPS results for C 1s, which also showed peaks corresponding to carbonate species like CO_3^{2-}. Figure 7f reveals that the sample containing the highest amount of cobalt tends to retain more carbonates.

Comparing the TGA profiles of the spent samples with those of fresh materials, similar peaks were still evident (Figure 9c,d). This indicates that the carbonates released during thermal degradation are residuals from the CaO precursor ($CaCO_3$), rather than from coke formation during the reaction. This is further evidenced by the similarity in the observed quantities of carbonates in both fresh and spent samples (allowing for some experimental variations). However, Figure S8 shows a more intense carbon peak after one adsorption-reaction cycle, whichcould be attributed to residual carbonates with a minimal contribution from coking mechanisms. The $Ce_{0.75}Co_{0.25}$ and $Ce_{0.50}Co_{0.50}$ samples also displayed an additional vibrational mode at 950 cm^{-1}, which was assigned to Si−OH/O^- stretching vibrations.[86−88] As per the literature,[89] this peak could stem from the formation of nickel phyllosilicates, which was attributed to binding between the nickel and bentonite clay. Based on the reactionary results shown in Figure 8, and the spectra shown in Figure 9it can be reasonably claimed that such carbonate retention might lead to lower activity for the samples with higher cobalt loading. In this way, it was therefore concluded from Figure 9a−e that—in addition to differences in activity stemming from the catalytic reducibility and oxygen availability that facilitate the redox (reduction−oxidation) reactions—the enhanced performance of CCN-1 can be attributed to, at least in part, retained carbonates over the cobalt phase, such as in CCN-3/Ca.

The best performance was observed in the CCN-1 sample, with its best overall balance of performance heuristics being observed at T = 700 °C, so the cyclic stability of this BFM was

https://doi.org/10.1021/jacsau.3c00553
JACS Au 2024, 4, 101−115

assessed over five adsorption-reaction cycles, as shown in Figure 10. Evidently, the performance of the sample equilibrated in the third cycle where the CO_2 adsorption capacity became constant. Across the entirety of the five cycles, however, it should be noted that the H_2 yield and selectivity—as well as the CH_4 and CO_2 conversions—remained almost perfectly constant (Figure 10b). The major alteration in the performance was a reduction in the level of CO_2 adsorption, as illustrated in Figure 10a. Given that this was the only variable showing a change, it suggests that the active sites for CO_2 adsorption were gradually compromised through repeated adsorption-reaction cycles, leading to a decreased level of capture over time. Importantly, this reduction in CO_2 adsorption did not substantially affect either the product yield or reactant conversion. This finding reaffirms the role of developing mixed metal oxide catalysts, which maintain a high density of surface electrons due to their metal reducibility and reactive oxygen species. As a result, minimal coke formation occurs, ensuring catalytic stability throughout multiple cycles. Such stability is imperative to the use of BFMs in industrial applications, and the stability of CCN-1/Ca with a 2.30 H_2/CO ratio at 700 °C—as well as its exceptionally high H_2 yield compared to other comparable literary sources, which range in value from 30 to 65%—[90−92] cement 3D printing as a facile means of generating structured honeycomb contactors.

4. CONCLUSIONS

In this study, a series of BFMs composed of CaO adsorbent and $Ce_{1-x}Co_xNiO_3$ perovskite-type oxide catalysts were structured via 3D printing and assessed for the first time for combined CO_2 capture and methane reforming to produce H_2. Characterizing the samples revealed that the cobalt content did not impact metallic dispersion, textural properties, or crystallinity but substantially affected redox properties, CO_2 and CaO binding strength, and oxygen species availability. To be specific, increasing the cobalt loading relative to ceria reduced the BFMs' reducibility and CO_2 adsorption/desorption reversibility. These effects translated to a reduced H_2 yield at higher cobalt loading upon assessing the samples for CO_2 capture and utilization at all three temperatures, thus revealing the best performance in the CCN-1/Ca sample that achieved 77% CO_2 conversion, 94% CH_4 conversion, 61% H_2 yield, and 2.30 H_2/CO ratio. This sample was thusly selected for cyclic assessment at a reaction temperature of 700 °C and showed minimal variability across five adsorption/reaction runs. In this context, the developed BFM monoliths demonstrated herein serve as a promising means through which mixed metal oxide BFMs can be manufactured, since these materials were both 3D-printed for the first time and also demonstrated stable cyclic performance for combined CO_2 capture and H_2 production.

ASSOCIATED CONTENT

Supporting Information

The Supporting Information is available free of charge at https://pubs.acs.org/doi/10.1021/jacsau.3c00553.

Estimation of adsorption-reaction parameters, reaction pathways, SEM and EDS mapping images of BFM monoliths, Rietveld refinement analysis (RIR) results using XRD, BET surface area and PSD profiles of BFM monoliths, high-resolution XPS spectra of C 1s for structured BFM monoliths, direct synthesis of hydrogen from CO_2 and methane over structured BFM monoliths at isothermal adsorption-reaction conditions, and TGA profiles and Raman spectra of fresh and spent BFM monoliths (PDF)

AUTHOR INFORMATION

Corresponding Authors

Ali A. Rownaghi − *National Energy Technology Laboratory, United States Department of Energy, Pittsburgh, Pennsylvania 15236, United States;* orcid.org/0000-0001-5228-5624; Email: ali.rownaghi@netl.doe.gov

Fateme Rezaei − *Linda and Bipin Doshi Department of Chemical and Biochemical Engineering, Missouri University of Science and Technology, Rolla, Missouri 65409-1230, United States; Department of Chemical, Environmental and Materials Engineering, University of Miami, Miami, Florida 33124, United States;* orcid.org/0000-0002-4214-4235; Email: fxr357@miami.edu

Authors

Khaled Baamran − *Linda and Bipin Doshi Department of Chemical and Biochemical Engineering, Missouri University of Science and Technology, Rolla, Missouri 65409-1230, United States*

Shane Lawson − *Linda and Bipin Doshi Department of Chemical and Biochemical Engineering, Missouri University of Science and Technology, Rolla, Missouri 65409-1230, United States*

Complete contact information is available at: https://pubs.acs.org/10.1021/jacsau.3c00553

Notes

The authors declare no competing financial interest.

ACKNOWLEDGMENTS

The authors acknowledge National Science Foundation internship program (NSF CBET-2316143) and the Electron Microscopy Core (EMC) at the University of Missouri Columbia for performing the SEM and EDS characterizations. The authors also acknowledge the materials research center (MRC) at Missouri University of Science and Technology for performing the XRD and XPS characterizations.

REFERENCES

(1) Chauvy, R.; Meunier, N.; Thomas, D.; De Weireld, G. Selecting Emerging CO_2 Utilization Products for Short-to Mid-Term Deployment. *Appl. Energy* **2019**, *236*, 662−680.

(2) Fawzy, S.; Osman, A. I.; Doran, J.; Rooney, D. W. Strategies for Mitigation of Climate Change: A Review. *Environ. Chem. Lett.* **2020**, *18*, 2069−2094.

(3) Anika, O. C.; Nnabuife, S. G.; Bello, A.; Okoroafor, R. E.; Kuang, B.; Villa, R. Prospects of Low and Zero-Carbon Renewable Fuels in 1.5-Degree Net Zero Emission Actualisation by 2050: A Critical Review. *Carbon Capture. Science & Technology* **2022**, *5*, No. 100072.

(4) Mac Dowell, N.; Fennell, P. S.; Shah, N.; Maitland, G. C. The Role of CO_2 Capture and Utilization in Mitigating Climate Change. *Nat. Clim Chang* **2017**, *7* (4), 243−249.

(5) Al-Mamoori, A.; Krishnamurthy, A.; Rownaghi, A. A.; Rezaei, F. Carbon Capture and Utilization Update. *Energy Technology* **2017**, *5* (6), 834−849.

(6) Bertram, C.; Luderer, G.; Creutzig, F.; Bauer, N.; Ueckerdt, F.; Malik, A.; Edenhofer, O. COVID-19-Induced Low Power Demand

and Market Forces Starkly Reduce CO_2 Emissions. *Nat. Clim Chang* **2021**, *11* (3), 193−196.
(7) Xing, F.; Nakaya, Y.; Yasumura, S.; Shimizu, K.; Furukawa, S. Ternary Platinum−Cobalt−Indium Nanoalloy on Ceria as a Highly Efficient Catalyst for the Oxidative Dehydrogenation of Propane Using CO_2. *Nat. Catal* **2022**, *5* (1), 55−65.
(8) Vogt, C.; Monai, M.; Kramer, G. J.; Weckhuysen, B. M. The Renaissance of the Sabatier Reaction and Its Applications on Earth and in Space. *Nat. Catal* **2019**, *2* (3), 188−197.
(9) Lawson, S.; Baamran, K.; Newport, K.; Garcia, E.; Jacobs, G.; Rezaei, F.; Rownaghi, A. A. Adsorption-Enhanced Bifunctional Catalysts for In Situ CO_2 Capture and Utilization in Propylene Production: A Proof-Of-Concept Study. *ACS Catal.* **2022**, *12* (22), 14264−14279.
(10) Lawson, S.; Baamran, K.; Newport, K.; Alghamadi, T.; Jacobs, G.; Rezaei, F.; Rownaghi, A. A. Integrated Direct Air Capture and Oxidative Dehydrogenation of Propane with CO_2 at Isothermal Conditions. *Appl. Catal., B* **2022**, *303*, No. 120907.
(11) Baamran, K.; Lawson, S.; Rownaghi, A. A.; Rezaei, F. Process Evaluation and Kinetic Analysis of 3D-Printed Monoliths Comprised of CaO and Cr/H-ZSM-5 in Combined CO_2 Capture-C_2H_6 Oxidative Dehydrogenation to C_2H_4. *Chemical Engineering Journal* **2022**, *435*, No. 134706.
(12) Sutthiumporn, K.; Maneerung, T.; Kathiraser, Y.; Kawi, S. CO_2 Dry-Reforming of Methane over $La_{0.8}Sr_{0.2}Ni_{0.8}M_{0.2}O_3$ Perovskite (M= Bi, Co, Cr, Cu, Fe): Roles of Lattice Oxygen on C−H Activation and Carbon Suppression. *Int. J. Hydrogen Energy* **2012**, *37* (15), 11195−11207.
(13) Bhavani, A. G.; Kim, W. Y.; Lee, J. S. Barium Substituted Lanthanum Manganite Perovskite for CO_2 Reforming of Methane. *ACS Catal.* **2013**, *3* (7), 1537−1544.
(14) Bhattar, S.; Abedin, M. A.; Kanitkar, S.; Spivey, J. J. A Review on Dry Reforming of Methane over Perovskite Derived Catalysts. *Catal. Today* **2021**, *365*, 2−23.
(15) Pan, X.; Jiao, F.; Miao, D.; Bao, X. Oxide−Zeolite-Based Composite Catalyst Concept That Enables Syngas Chemistry beyond Fischer−Tropsch Synthesis. *Chem. Rev.* **2021**, *121* (11), 6588−6609.
(16) Jiao, F.; Pan, X.; Gong, K.; Chen, Y.; Li, G.; Bao, X. Shape-Selective Zeolites Promote Ethylene Formation from Syngas via a Ketene Intermediate. *Angew. Chem., Int. Ed.* **2018**, *57* (17), 4692−4696.
(17) Marcinkowski, M. D.; Darby, M. T.; Liu, J.; Wimble, J. M.; Lucci, F. R.; Lee, S.; Michaelides, A.; Flytzani-Stephanopoulos, M.; Stamatakis, M.; Sykes, E. C. H. Pt/Cu Single-Atom Alloys as Coke-Resistant Catalysts for Efficient C−H Activation. *Nat. Chem.* **2018**, *10* (3), 325−332.
(18) Zhu, Q.; Zhou, H.; Wang, L.; Wang, L.; Wang, C.; Wang, H.; Fang, W.; He, M.; Wu, Q.; Xiao, F.-S. Enhanced CO_2 Utilization in Dry Reforming of Methane Achieved through Nickel-Mediated Hydrogen Spillover in Zeolite Crystals. *Nat. Catal.* **2022**, *5*, 1030−1037.
(19) Mette, K.; Kühl, S.; Düdder, H.; Kähler, K.; Tarasov, A.; Muhler, M.; Behrens, M. Stable Performance of Ni Catalysts in the Dry Reforming of Methane at High Temperatures for the Efficient Conversion of CO_2 into Syngas. *ChemCatChem.* **2014**, *6* (1), 100−104.
(20) Xia, X.; Chang, W.; Cheng, S.; Huang, C.; Hu, Y.; Xu, W.; Zhang, L.; Jiang, B.; Sun, Z.; Zhu, Y.; Wang, X. Oxygen Activity Tuning via FeO_6 Octahedral Tilting in Perovskite Ferrites for Chemical Looping Dry Reforming of Methane. *ACS Catal.* **2022**, *12*, 7326−7335.
(21) Rabelo-Neto, R. C.; Sales, H. B. E.; Inocêncio, C. V. M.; Varga, E.; Oszko, A.; Erdohelyi, A.; Noronha, F. B.; Mattos, L. V. CO_2 Reforming of Methane over Supported $LaNiO_3$ Perovskite-Type Oxides. *Appl. Catal., B* **2018**, *221*, 349−361.
(22) Chang, H.; Bjørgum, E.; Mihai, O.; Yang, J.; Lein, H. L.; Grande, T.; Raaen, S.; Zhu, Y.-A.; Holmen, A.; Chen, D. Effects of Oxygen Mobility in La−Fe-Based Perovskites on the Catalytic Activity and Selectivity of Methane Oxidation. *ACS Catal.* **2020**, *10* (6), 3707−3719.
(23) Bian, Z.; Wang, Z.; Jiang, B.; Hongmanorom, P.; Zhong, W.; Kawi, S. A Review on Perovskite Catalysts for Reforming of Methane to Hydrogen Production. *Renewable and Sustainable Energy Reviews* **2020**, *134*, No. 110291.
(24) Sastre, D.; Serrano, D. P.; Pizarro, P.; Coronado, J. M. Chemical Insights on the Activity of $La_{1-X}Sr_xFeO_3$ Perovskites for Chemical Looping Reforming of Methane Coupled with CO_2-Splitting. *J. CO_2 Util.* **2019**, *31*, 16−26.
(25) Li, H.; Hao, C.; Tian, J.; Wang, S.; Zhao, C. Ultra-Durable Ni-Ir/$MgAl_2O_4$ Catalysts for Dry Reforming of Methane Enabled by Dynamic Balance between Carbon Deposition and Elimination. *Chem. Catalysis* **2022**, *2* (7), 1748−1763.
(26) Long, D. B.; Hau, B. T.; Thuy Van, N. T.; Anh, N. P.; Gia-Thien Ho, T.; Anh, H. C.; Phuong, P. H.; Huy, C. D.; Tri, N.; Loc, L. C. High Active and Coke-Resistant $CeNiO_3$-Based Catalyst for Methane Bi-Reforming. *Journal of Science: Advanced Materials and Devices* **2023**, *8* (3), No. 100610.
(27) Saeed Baamran, K.; Tahir, M. Thermodynamic Investigation and Experimental Analysis on Phenol Steam Reforming towards Enhanced H_2 Production over Structured Ni/$ZnTiO_3$ Nanocatalyst. *Energy Convers Manag* **2019**, *180*, 796−810.
(28) Baamran, K. S.; Tahir, M. Ni-Embedded TiO_2-$ZnTiO_3$ Reducible Perovskite Composite with Synergistic Effect of Metal/Support towards Enhanced H_2 Production via Phenol Steam Reforming. *Energy Convers. Manage.* **2019**, *200*, No. 112064.
(29) Huang, C.; Wu, J.; Chen, Y.-T.; Tian, M.; Rykov, A. I.; Hou, B.; Lin, J.; Chang, C.-R.; Pan, X.; Wang, J.; Wang, A; Wang, X. In Situ Encapsulation of Iron(0) for Solar Thermochemical Syngas Production over Iron-Based Perovskite Material. *Commun. Chem.* **2018**, *1* (1), 55.
(30) Wang, Y.; Chen, X.; Shi, H.; Lercher, J. A. Catalytic Reforming of Methane with H_2S via Dynamically Stabilized Sulfur on Transition Metal Oxides and Sulfides. *Nat. Catal.* **2023**, *6*, 204−214.
(31) Chai, S. Y. W.; Ngu, L. H.; How, B. S. Review of Carbon Capture Absorbents for CO_2 Utilization. *Greenhouse Gases: Science and Technology* **2022**, *12* (3), 394−427.
(32) Ghoniem, A. F. Needs, Resources and Climate Change: Clean and Efficient Conversion Technologies. *Prog. Energy Combust. Sci.* **2011**, *37* (1), 15−51.
(33) Mikhelkis, L.; Govindarajan, V. Techno-Economic and Partial Environmental Analysis of Carbon Capture and Storage (CCS) and Carbon Capture, Utilization, and Storage (CCU/S): Case Study from Proposed Waste-Fed District-Heating Incinerator in Sweden. *Sustainability* **2020**, *12* (15), 5922.
(34) Duyar, M. S.; Trevino, M. A. A.; Farrauto, R. J. Dual Function Materials for CO_2 Capture and Conversion Using Renewable H_2. *Appl. Catal., B* **2015**, *168*, 370−376.
(35) Magzoub, F.; Li, X.; Al-Darwish, J.; Rezaei, F.; Rownaghi, A. A. 3D-printed ZSM-5 monoliths with metal dopants for methanol conversion in the presence and absence of carbon dioxide. *Appl. Catal., B* **2019**, *245*, 486−495.
(36) Magzoub, F.; Li, X.; Al-Darwish, J.; Rezaei, F.; Rownaghi, A. A. Directly Printed Oxide/ZSM-5 Bifunctional Catalysts for Methanol Conversion to Dimethyl Ether with Exceptional Stability, Conversion, and Selectivity. *Energy Fuels* **2021**, *35* (3), 2619−2629.
(37) Arellano-Trevino, M. A.; Kanani, N.; Jeong-Potter, C. W.; Farrauto, R. J. Bimetallic Catalysts for CO_2 Capture and Hydrogenation at Simulated Flue Gas Conditions. *Chemical Engineering Journal* **2019**, *375*, No. 121953.
(38) Omodolor, I. S.; Otor, H. O.; Andonegui, J. A.; Allen, B. J.; Alba-Rubio, A. C. Dual-Function Materials for CO_2 Capture and Conversion: A Review. *Ind. Eng. Chem. Res.* **2020**, *59* (40), 17612−17631.
(39) Sun, H.; Zhang, Y.; Guan, S.; Huang, J.; Wu, C. Direct and Highly Selective Conversion of Captured CO_2 into Methane through Integrated Carbon Capture and Utilization over Dual Functional Materials. *J. CO_2 Util.* **2020**, *38*, 262−272.

https://doi.org/10.1021/jacsau.3c00553
JACS Au 2024, 4, 101−115

(40) Guo, Y.; Wang, G.; Yu, J.; Huang, P.; Sun, J.; Wang, R.; Wang, T.; Zhao, C. Tailoring the Performance of Ni-CaO Dual Function Materials for Integrated CO_2 Capture and Conversion by Doping Transition Metal Oxides. *Sep Purif Technol.* **2023**, *305*, No. 122455.
(41) Onrubia-Calvo, J. A.; Bermejo-López, A.; Pereda-Ayo, B.; González-Marcos, J. A.; González-Velasco, J. R. Ca Doping Effect on the Performance of $La_{1-X}Ca_xNiO_3/CeO_2$-Derived Dual Function Materials for CO_2 Capture and Hydrogenation to Methane. *Appl. Catal., B* **2023**, *321*, No. 122045.
(42) Gelles, T.; Lawson, S.; Rownaghi, A. A.; Rezaei, F. Recent advances in development of amine functionalized adsorbents for CO_2 capture. *Adsorption* **2020**, *26*, 5−50.
(43) Lawson, S.; Li, X.; Thakkar, H.; Rownaghi, A. A.; Rezaei, F. Recent Advances in 3D Printing of Structured Materials for Adsorption and Catalysis Applications. *Chem. Rev.* **2021**, *121* (10), 6246−6291.
(44) Lawson, S.; Baamran, K.; Newport, K.; Rezaei, F.; Rownaghi, A. A. Formulation and Processing of Dual Functional Adsorbent/Catalyst Structured Monoliths Using an Additively Manufactured Contactor for Direct Capture/Conversion of CO_2 with Cogeneration of Ethylene. *Chemical Engineering Journal* **2022**, *431*, No. 133224.
(45) Lawson, S.; Baamran, K.; Newport, K.; Rezaei, F.; Rownaghi, A. Screening of Adsorbent/Catalyst Composite Monoliths for Carbon Capture-Utilization and Ethylene Production. *ACS Appl. Mater. Interfaces* **2021**, *13* (46), 55198−55207.
(46) Baamran, K.; Rownaghi, A. A.; Rezaei, F. Direct Synthesis of Ethylene and Hydrogen from CO_2 and Ethane over a Bifunctional Structured CaO/Cr_2O_3-V_2O_5/ZSM-5 Adsorbent/Catalyst Monolith. *ACS Sustain Chem. Eng.* **2023**, *11* (3), 1006−1018.
(47) Agbi, T.; Lo, W. S.; Baamran, K.; Ryu, T.; Cheung, C.; Rezaei, F.; Hermans, I. 3D-Printed Boron Nitride Catalytic Monoliths for Oxidative Dehydrogenation of Propane. *Top Catal* **2023**, *66*, 1152−1160.
(48) Ding, H.; Xu, Y.; Luo, C.; Wang, Q.; Shen, C.; Xu, J.; Zhang, L. A Novel Composite Perovskite-Based Material for Chemical-Looping Steam Methane Reforming to Hydrogen and Syngas. *Energy Convers Manag* **2018**, *171*, 12−19.
(49) Choi, S. O.; Penninger, M.; Kim, C. H.; Schneider, W. F.; Thompson, L. T. Experimental and Computational Investigation of Effect of Sr on NO Oxidation and Oxygen Exchange for $La_{1-x}Sr_xCoO_3$ Perovskite Catalysts. *ACS Catal.* **2013**, *3* (12), 2719−2728.
(50) Thakkar, H.; Eastman, S.; Hajari, A.; Rownaghi, A. A.; Knox, J. C.; Rezaei, F. 3D-Printed Zeolite Monoliths for CO_2 Removal from Enclosed Environments. *ACS Appl. Mater. Interfaces* **2016**, *8* (41), 27753−27761.
(51) Lawson, S.; Rezaei, F. Effects of Process Parameters on CO_2/H_2 Separation Performance of 3D-Printed MOF-74 Monoliths. *ACS Sustain Chem. Eng.* **2021**, *9*, 10902−10912.
(52) Thakkar, H.; Lawson, S.; Rownaghi, A. A.; Rezaei, F. Development of 3D-Printed Polymer-Zeolite Composite Monoliths for Gas Separation. *Chemical Engineering Journal* **2018**, *348*, 109−116.
(53) Newport, K.; Baamran, K.; Rownaghi, A. A.; Rezaei, F. Magnetic-Field Assisted Gas Desorption from Fe_2O_3/Zeolite 13X Sorbent Monoliths for Biogas Upgrading. *Ind. Eng. Chem. Res.* **2022**, *61* (51), 18843−18853.
(54) Lawson, S.; Farsad, A.; Rezaei, F.; Ludlow, D.; Rownaghi, A. A. Direct Ink Writing of Metal Oxide/H-ZSM-5 Catalysts for *n*-Hexane Cracking: A New Method of Additive Manufacturing with High Metal Oxide Loading. *ACS Appl. Mater. Interfaces* **2021**, *13*, 781−794.
(55) Lawson, S.; Farsad, A.; Adebayo, B.; Newport, K.; Schueddig, K.; Lowrey, E.; Polo-Garzon, F.; Rezaei, F.; Rownaghi, A. A. A Novel Method of 3D Printing High-Loaded Oxide/H-ZSM-5 Catalyst Monoliths for Carbon Dioxide Reduction in Tandem with Propane Dehydrogenation. *Adv. Sustain Syst* **2021**, *5* (3), No. 2000257.
(56) Jayakumar, G.; Irudayaraj, A. A.; Raj, A. D. Particle Size Effect on the Properties of Cerium Oxide (CeO_2) Nanoparticles Synthesized by Hydrothermal Method. *Mech., Mater. Sci. Eng. J.* **2017**, *9* (1), 1−6.
(57) Das, S.; Bhattar, S.; Liu, L.; Wang, Z.; Xi, S.; Spivey, J. J.; Kawi, S. Effect of Partial Fe Substitution in $La_{0.9}Sr_{0.1}NiO_3$ Perovskite-Derived Catalysts on the Reaction Mechanism of Methane Dry Reforming. *ACS Catal.* **2020**, *10* (21), 12466−12486.
(58) Broda, M.; Kierzkowska, A. M.; Baudouin, D.; Imtiaz, Q.; Coperet, C.; Muller, C. R. Sorbent-Enhanced Methane Reforming over a Ni−Ca-Based, Bifunctional Catalyst Sorbent. *ACS Catal.* **2012**, *2* (8), 1635−1646.
(59) Fang, Y.; Wang, X.; Chen, Y.; Dai, L. $NiCo_2O_4$ nanoparticles: an efficient and magnetic catalyst for Knoevenagel condensation. *J. Zhejiang Univ., Sci., A* **2020**, *21*, 74−84.
(60) Wang, T.; Qiu, L.; Li, H.; Zhang, C.; Sun, Y.; Xi, S.; Ge, J.; Xu, Z. J.; Wang, C. Facile Synthesis of Palladium Incorporated $NiCo_2O_4$ Spinel for Low Temperature Methane Combustion: Activate Lattice Oxygen to Promote Activity. *J. Catal.* **2021**, *404*, 400−410.
(61) Alghamdi, T.; Baamran, K. S.; Okoronkwo, M. U.; Rownaghi, A. A.; Rezaei, F. Metal-Doped K−Ca Double Salts with Improved Capture Performance and Stability for High-Temperature CO_2 Adsorption. *Energy Fuels* **2021**, *35* (5), 4258−4266.
(62) Kim, S.; Park, C. B. Dopamine-Induced Mineralization of Calcium Carbonate Vaterite Microspheres. *Langmuir* **2010**, *26* (18), 14730−14736.
(63) Achour, A.; Arman, A.; Islam, M.; Zavarian, A. A.; Basim Al-Zubaidi, A.; Szade, J. Synthesis and Characterization of Porous CaCO3 Micro/Nano-Particles. *Eur. Phys. J. Plus* **2017**, *132* (6), 267.
(64) de Oliveira, C. I. R.; Rocha, M. C. G.; Da Silva, A. L. N.; Bertolino, L. C. Characterization of Bentonite Clays from Cubati, Paraíba (Northeast of Brazil). *Cerâmica* **2016**, *62*, 272−277.
(65) Ambroz, F.; Macdonald, T. J.; Martis, V.; Parkin, I. P. Evaluation of the BET Theory for the Characterization of Meso and Microporous MOFs. *Small Methods* **2018**, *2* (11), No. 1800173.
(66) Al-Darwish, J.; Senter, M.; Lawson, S.; Rownaghi, A. A.; Rezaei, F. Ceria nanostructured catalysts for conversion of methanol and carbon dioxide to dimethyl carbonate. *Energy & Catalysis Today* **2020**, *350*, 120−126.
(67) Lanre, M. S.; Abasaeed, A. E.; Fakeeha, A. H.; Ibrahim, A. A.; Alquraini, A. A.; AlReshaidan, S. B.; Al-Fatesh, A. S. Modification of $CeNi_{0.9}Zr_{0.1}O_3$ Perovskite Catalyst by Partially Substituting Yttrium with Zirconia in Dry Reforming of Methane. *Materials* **2022**, *15* (10), 3564.
(68) Zhang, D.; Xie, H.; Chen, S.; Zhou, G. Porous CoCe Composite Catalyst Prepared by Hydrothermal Assisted Soft Template Method for CH_4/CO_2 Dry Reforming. *Fuel* **2022**, *327*, No. 125105.
(69) Das, S.; Lim, K. H.; Gani, T. Z. H.; Aksari, S.; Kawi, S. Bi-Functional CeO_2 Coated NiCo-MgAl Core-Shell Catalyst with High Activity and Resistance to Coke and H_2S Poisoning in Methane Dry Reforming. *Appl. Catal., B* **2023**, *323*, No. 122141.
(70) Lyu, Y.; Jocz, J.; Xu, R.; Stavitski, E.; Sievers, C. Nickel Speciation and Methane Dry Reforming Performance of Ni/$Ce_xZr_{1-x}O_2$ Prepared by Different Synthesis Methods. *ACS Catal.* **2020**, *10* (19), 11235−11252.
(71) Zhao, K.; Chen, J.; Li, H.; Zheng, A.; Huang, Z.; Wei, G.; Zhao, Z.; Wang, X. Investigation of the Relationship between Electronic Properties and Reactivity of 3DOM $LaFe_{1-X}Co_xO_3$ for Methane Reforming to Produce Syngas. *Int. J. Energy Res.* **2019**, *43* (13), 7120−7134.
(72) Valderrama, G.; Kiennemann, A.; Goldwasser, M. R. La-Sr-Ni-Co-O Based Perovskite-Type Solid Solutions as Catalyst Precursors in the CO_2 Reforming of Methane. *J. Power Sources* **2010**, *195* (7), 1765−1771.
(73) Mallikarjun, G.; Sagar, T. V.; Swapna, S.; Raju, N.; Chandrashekar, P.; Lingaiah, N. Hydrogen Rich Syngas Production by Bi-Reforming of Methane with CO_2 over Ni Supported on CeO_2-SrO Mixed Oxide Catalysts. *Catal. Today* **2020**, *356*, 597−603.
(74) Lima, S. M.; Assaf, J. M.; Peña, M. A.; Fierro, J. L. G. Structural Features of $La_{1-X}Ce_xNiO_3$ Mixed Oxides and Performance for the Dry Reforming of Methane. *Appl. Catal., A* **2006**, *311*, 94−104.

https://doi.org/10.1021/jacsau.3c00553
JACS Au 2024, 4, 101−115

(75) Xiong, J.; Yang, J.; Chi, X.; Wu, K.; Song, L.; Li, T.; Zhao, Y.; Huang, H.; Chen, P.; Wu, J.; Chen, L.; Fu, M.; Ye, D. Pd-Promoted Co_2NiO_4 with Lattice Co-O-Ni and Interfacial Pd-O Activation for Highly Efficient Methane Oxidation. *Appl. Catal., B* **2021**, *292*, No. 120201.
(76) Hu, Q.; Yue, B.; Shao, H.; Yang, F.; Wang, J.; Wang, Y.; Liu, J. Facile Syntheses of Cerium-Based $CeMO_3$ (M = Co, Ni, Cu) Perovskite Nanomaterials for High-Performance Supercapacitor Electrodes. *J. Mater. Sci.* **2020**, *55* (20), 8421−8434.
(77) Maridevaru, M.; Aljafari, B.; Anandan, S. Synergistic Impacts of Sonolysis Aided Photocatalytic Degradation of Water Pollutant over Perovskite-Type $CeNiO_3$ Nanospheres. *New J. Chem.* **2022**, *46* (21), 10117−10127.
(78) Liang, D.; Wang, Y.; Chen, M.; Xie, X.; Li, C.; Wang, J.; Yuan, L. Dry Reforming of Methane for Syngas Production over Attapulgite-Derived MFI Zeolite Encapsulated Bimetallic Ni-Co Catalysts. *Appl. Catal., B* **2023**, *322*, No. 122088.
(79) Wang, N.; Shen, K.; Huang, L.; Yu, X.; Qian, W.; Chu, W. Facile Route for Synthesizing Ordered Mesoporous Ni−Ce−Al Oxide Materials and Their Catalytic Performance for Methane Dry Reforming to Hydrogen and Syngas. *ACS Catal.* **2013**, *3* (7), 1638−1651.
(80) Wang, Z.; Wu, P.; Zou, X.; Wang, S.; Du, L.; Ouyang, T.; Liu, Z. Q. Optimizing the Oxygen-Catalytic Performance of Zn−Mn−Co Spinel by Regulating the Bond Competition at Octahedral Sites. *Adv. Funct Mater.* **2023**, *33* (16), No. 2214275.
(81) Huang, H.; Li, X.; Wang, J.; Dong, F.; Chu, P. K.; Zhang, T.; Zhang, Y. Anionic Group Self-Doping as a Promising Strategy: Band-Gap Engineering and Multi-Functional Applications of High-Performance CO_3^{2-}-Doped $Bi_2O_2CO_3$. *ACS Catal.* **2015**, *5* (7), 4094−4103.
(82) Krödel, M.; Landuyt, A.; Abdala, P. M.; Müller, C. R. Mechanistic Understanding of CaO-Based Sorbents for High-Temperature CO_2 Capture: Advanced Characterization and Prospects. *ChemSusChem* **2020**, *13* (23), 6259−6272.
(83) Zhao, K.; Shen, Y.; Huang, Z.; He, F.; Wei, G.; Zheng, A.; Li, H.; Zhao, Z. Different Oxidation Routes for Lattice Oxygen Recovery of Double-Perovskite Type Oxides $LaSrFeCoO_6$ as Oxygen Carriers for Chemical Looping Steam Methane Reforming. *Journal of energy chemistry* **2017**, *26* (3), 501−509.
(84) Li, R.-J.; Yu, C.-C.; Ji, W.-J.; Shen, S.-K. Methane Oxidation to Synthesis Gas Using Lattice Oxygen in $La_{1-X}Sr_xFeO_3$ Perovskite Oxides Instead of Molecular Oxygen. *Stud. Surf. Sci. Catal.* **2004**, *147*, 199−204.
(85) Wang, H.; Dong, X.; Zhao, T.; Yu, H.; Li, M. Dry Reforming of Methane over Bimetallic Ni-Co Catalyst Prepared from La $(Co_xNi_{1-x})_{0.5}Fe_{0.5}O_3$ Perovskite Precursor: Catalytic Activity and Coking Resistance. *Appl. Catal., B* **2019**, *245*, 302−313.
(86) Amin, M. H. Relationship between the Pore Structure of Mesoporous Silica Supports and the Activity of Nickel Nanocatalysts in the CO_2 Reforming of Methane. *Catalysts* **2020**, *10* (1), 51.
(87) Li, J. F.; Xia, C.; Au, C. T.; Liu, B. S. Y_2O_3-Promoted NiO/SBA-15 Catalysts Highly Active for CO_2/CH_4 Reforming. *Int. J. Hydrogen Energy* **2014**, *39* (21), 10927−10940.
(88) Lehmann, T.; Wolff, T.; Hamel, C.; Veit, P.; Garke, B.; Seidel-Morgenstern, A. Physico-Chemical Characterization of Ni/MCM-41 Synthesized by a Template Ion Exchange Approach. *Microporous Mesoporous Mater.* **2012**, *151*, 113−125.
(89) Majewski, A. J.; Wood, J.; Bujalski, W. Nickel−Silica Core@Shell Catalyst for Methane Reforming. *Int. J. Hydrogen Energy* **2013**, *38* (34), 14531−14541.
(90) Das, S.; Jangam, A.; Jayaprakash, S.; Xi, S.; Hidajat, K.; Tomishige, K.; Kawi, S. Role of Lattice Oxygen in Methane Activation on Ni-Phyllosilicate@$Ce_{1-X}Zr_xO_2$ Core-Shell Catalyst for Methane Dry Reforming: Zr Doping Effect, Mechanism, and Kinetic Study. *Appl. Catal., B* **2021**, *290*, No. 119998.
(91) Al-Fatesh, A. S.; Chaudhary, M. L.; Fakeeha, A. H.; Ibrahim, A. A.; Al-Mubaddel, F.; Kasim, S. O.; Albaqmaa, Y. A.; Bagabas, A. A.; Patel, R.; Kumar, R. Role of Mixed Oxides in Hydrogen Production through the Dry Reforming of Methane over Nickel Catalysts Supported on Modified γ-Al_2O_3. *Processes* **2021**, *9* (1), 157.
(92) Patel, R.; Fakeeha, A. H.; Kasim, S. O.; Sofiu, M. L.; Ibrahim, A. A.; Abasaeed, A. E.; Kumar, R.; Al-Fatesh, A. S. Optimizing Yttria-Zirconia Proportions in Ni Supported Catalyst System for H_2 Production through Dry Reforming of Methane. *Molecular Catalysis* **2021**, *510*, No. 111676.

https://doi.org/10.1021/jacsau.3c00553
JACS Au 2024, 4, 101−115